Application of image analysis and image simulation for quantitative characterization of scale spallation during cyclic oxidation of a Pt-aluminide coating

Jacques Lacaze *, Maarten Lupker, Nadia Vialas, Daniel Monceau [1]

CIRIMAT, UMR 5085, ENSIACET, 31077 Toulouse cedex 4, France

Abstract

An image analysis and simulation of the spalled alumina areas at the surface of a Pt modified β-NiAl aluminide coating RT22 during cyclic oxidation in air is presented. The size distribution of the freshly spalled areas and of the unspalled zones is studied for the same coating deposited on three different nickel base superalloys which were exposed to various numbers of 300 h cycles at 1050 °C (up to 10,500 h) in a previous study [Vialas N, Monceau D. Oxid Metals, submitted for publication]. It is shown for this coating that the distribution of the freshly spalled area depends on the nature of the coated substrate and on the number of cycles. It is also shown that spallation of these three systems can be simulated by a two-parameter model which describes the spalling during the cooling step as successive microspalling events through nucleation and growth processes. This approach is consistent with previous in-situ observations and allows the introduction of a time-dependent damaging process in the models of cyclic oxidation kinetics.

Keywords: A. Nickel aluminides, based on NiAl; B. Oxidation; C. Coatings; D. Aero-engine components

1. Introduction

One of the causes for degradation of alloys in high temperature applications is the combined effects of oxidizing atmosphere and thermal cycling. These conditions lead chromia or alumina-forming alloys to oxidize at a faster rate than under isothermal conditions, because spalling of the protective oxide scale leads to repeated oxidation of the bare metal surface [2]. Consumption of the alloying elements by oxidation is then enhanced with the consequence of accelerated breakaway (i.e. formation of less protective oxides) and faster alloy microstructure evolution (e.g. near surface gamma–prime dissolution during Ni-based superalloy oxidation, or β-NiAl dissolution during NiAl-based diffusion coating oxidation). In addition, deterioration of mechanical properties may result from microstructural evolution or even from dynamic coupling between creep and oxidation [3].

Scale spalling results from the combination of a weak metal/oxide interface with mechanical stresses, namely 'growth stress' and stress induced by thermal-expansion coefficient mismatch between alloy and oxide [4]. Experimental data show that scale spalling depends on many factors such as surface roughness, surface preparation, material composition and segregation at the metal–oxide interface, cycle amplitude and duration (e.g. [4–6]). Despite this complex behavior, the kinetics of the spalling phenomena needs to be modeled in order to produce phenomenological laws for the time of life (TOL) modeling of parts used in high temperature applications, together, and sometimes in interaction with, creep, fatigue, erosion, diffusion, microstructure evolution, and high temperature corrosion laws. This demand for time of life modeling has led to simplified kinetics models which can be used for specific applications [7–13]. Better mechanistic understanding [4,5,14–17] of spalling needs to be developed in order to extend the application of kinetic models. A preliminary step in this direction is to improve description and quantification of the experimental results in order to test and develop the mechanistic and kinetic models.

* Corresponding author. Fax: +33 5 6288 5663.
E-mail address: jacques.lacaze@ensiacet.fr (J. Lacaze).
[1] Present address: School of Materials Science and Engineering, University of New South Wales, Sydney, Australia.

doi:10.1016/j.intermet.2005.08.007

The present study provides a method for the characterization of spalled specimens using image analysis and proposes a model for the damage mechanism which is illustrated through image simulation. The model represents experimental spalling data with two parameters, and describes spalling as a time damaging process and not only as a process which depends on growth on the oxide scale thickness. The characterization performed here improves the commonly used description of spalling, i.e. the simple use of the mass fraction or of the surface area fraction which spalls at each cycle. The model could lead to a better understanding of the effect of the dwell time during cyclic oxidation experiments which does not follow a simple rule [6,18], and could help to describe phenomena such as 'desktop spalling' (or 'delayed spalling') which is well known from experiment (e.g. with thermal barrier coating systems) and which was recently measured using cyclic thermogravimetry during interrupted cyclic oxidation of NiAl single crystal [19].

2. Materials, experimental procedures and summary of previous materials characterizations

The detailed description of the materials and of their microstructure before and after oxidation can be found along with a description of the experimental procedures elsewhere [1]. The main features which are useful for the present image analysis study are recalled in the following.

Three Ni-base superalloys were used as substrates: single grain alloys CMSX-4™ and SCB444™ [20] and a polycrystalline alloy IN792™ containing 0.5 wt.% Hf. Disc specimens (9 mm in diameter and 2 mm thick) were coated with a Pt-modified aluminide diffusion coating RT22™ and heat treated by Chromalloy-France. The arithmetic roughness R_a (i.e. the average of the distance between the surface and the virtual mean flat surface) of the three systems (i.e. the three coated superalloys) was measured before oxidation with an optical microscope equipped with a ZIGO Newview 100 interferometer with 1 nm in depth resolution. R_a was found not to depend on the superalloy substrate, being 1.3 μm for RT22/CMSX-4, 1.5 μm for RT22/SCB and 1.3 μm for RT22/IN792. Also, slight undulations of the surfaces with a wavelength of about 20 μm were observed by scanning electron microscopy.

Specimens were submitted to cyclic oxidation in the 'as-coated' state, without any polishing or grit blasting. The specimens were hung with a platinum–rhodium wire on an alumina rod to be introduced in a Carbolite furnace at 1050 °C in still laboratory air. Each cycle consisted of a heating stage at a rate of 3 °C/s, an isothermal 300 h long exposure at 1050 °C, and a cooling stage. During cooling, specimens were removed from the furnace to be placed in front of fans at room temperature, which results in an initial cooling rate of 9 °C/s. For each cycle, the net mass gain per unit area (NMG) of all the samples was recorded using a Sartorius microbalance with 10 μg accuracy. After 6, 17 and 35 cycles of 300 h, one sample of each material was removed for a full characterization. The oxide phases present in the scale were identified using a Seiffert X-Ray diffraction apparatus (XRD) and with a PGT™ energy dispersive X-Ray spectrometry system (EDS).

Images were recorded using a scanning electron microscope from LEO operated at 15 kV.

In the previous work [1] it was demonstrated that the cyclic oxidation kinetics of the Pt-modified NiAl coating RT22™ depends on the nature of the superalloy substrate. Indeed, despite a superior cyclic oxidation of the CMSX-4 superalloy itself when compared to SCB and IN792 alloys, it was shown that the system RT22/IN792 has a superior long term cyclic oxidation resistance at 1050 °C compared to the other two systems. This observation was explained by the phase transformations which occurred in the coating and which depend on the chemical composition of the superalloy substrate. In the three systems, the beta (NiAl) phase transformed to gamma prime (Ni_3Al) and eventually gamma (Ni). The transformation from beta to gamma prime phase results in a large volume contraction, which was quantitatively analyzed. It was shown that in the RT22/IN792, the transformation front was uniform and parallel to the surface and consequently that surface recession could accommodate the volume change. But in the two other systems RT22/CMSX-4 and RT22/SCB, it was shown that the phase transformation was localized at coating grain boundaries, with a transformation front perpendicular to the sample surface. Here, the surface recession cannot accommodate the reduction in volume and deep voids appeared at grain boundaries of the coating, below the oxide scale. This kind of void had been previously observed on similar systems [21]. A quantitative agreement between the volume of these pores and the volume reduction due to the phase transformation was found [1]. From the correlation between the presence of such voids and the larger amount of spalling in these two systems, it was inferred that the voids could act as nucleation sites for spalling. This hypothesis was also supported by the XRD and EDX characterizations of the oxide scale. Indeed, the small differences observed in the oxide scale composition could not explain the best cyclic oxidation resistance of the RT22/IN792 system as compared to the two others. The SEM images in Fig. 1 give an example of the surfaces of the RT22 coating on the three different superalloys, after 35 cycles (i.e. 15,600 h at 1050 °C). As mentioned earlier, many voids were observed at the metal surface in RT22/CMSX-4 and RT22/SCB systems after 6, 17 and 35 cycles of 300 h at 1050 °C. An example of such voids surrounded by metallic matrix is shown in Fig. 1d.

As the lower cyclic oxidation resistance of the RT22/CMSX-4 and RT22/SCB systems with respect to the system RT22/IN792 was thought to be linked to the formation of voids under the oxide scale leading to enhanced spalling, it was decided to perform a quantification of the spall areas using image analysis. Thus, in the present work, backscattered electrons were used in such a way that the brightest areas, which correspond to the areas spalled during the last cycle, appeared highly contrasted with respect to darker zones, which are covered with oxide scale. Grey tone numerical images were coded with 256 grey levels, from 0 (dark) to 255 (white) and were 701×1001 pixels in size implemented on a square grid.

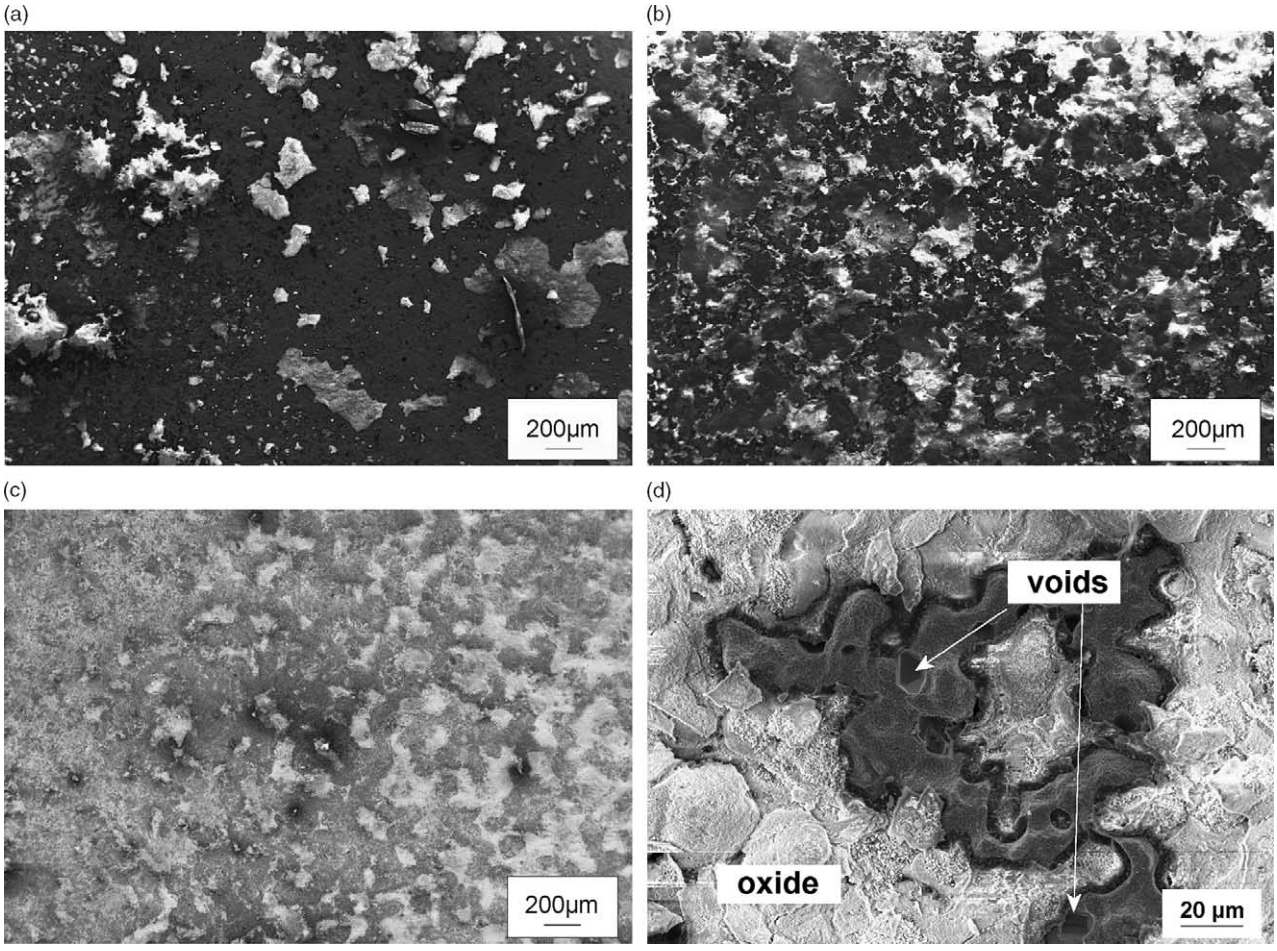

Fig. 1. SEM secondary electron images (SEI) of the surface of samples (a) RT22/CMSX-4 (b) RT22/IN792 (c) RT22/SCB after 35 cycles of 300 h at 1050 °C in air. Bright areas are the residual oxide and dark areas correspond to spalled zones. In the image (d) facetted voids can be seen on spalled areas (RT22/SCB after 6 cycles of 300 h at 1050 °C).

Images to be analysed were recorded at an enlargement of ×30 but one was at ×40. The corresponding pixel size is thus 3.8 µm for the former and 2.85 µm for the latter. Image analysis as well as image simulations were performed with APHELION software from ADCIS (Caen, France).

3. Presentation of the experimental images

On the secondary electron images of oxidized samples, presented in Fig. 1, the spalled zones appear dark and the remaining oxide scale appears bright. Fig. 2 shows the same

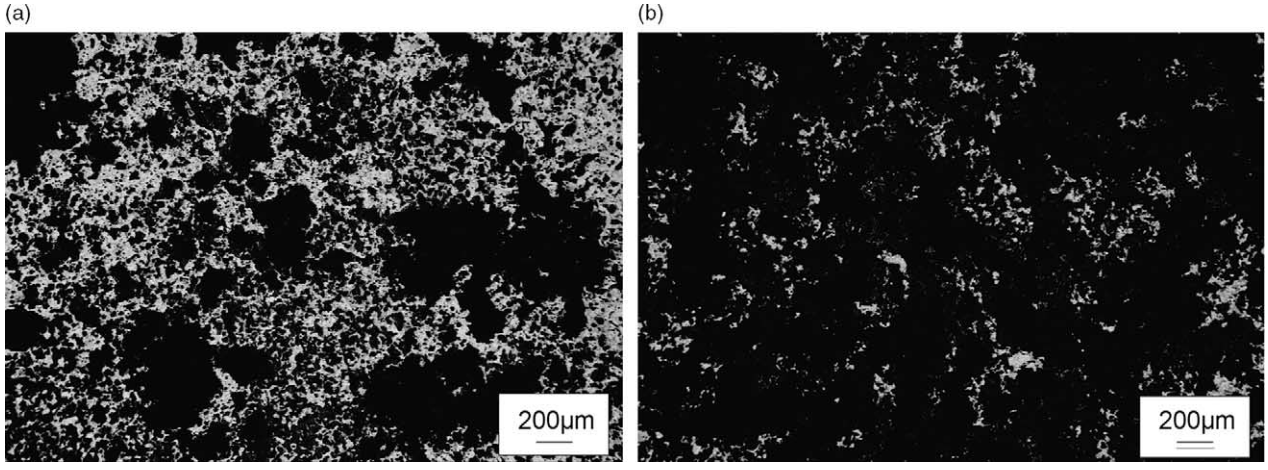

Fig. 2. SEM images (backscattered electrons) of the surface of samples (a) RT22/CMSX-4 and (b) RT22/IN792 after 35 cycles (same area as Fig. 1b). Lighter areas are spalled zones.

sample surfaces as in Fig. 1a and b, making use of backscattered electrons (BSE) to get a high average atomic number contrast between spalled and unspalled areas. Indeed, the oxide scale being much lighter than the nickel-base coating, it appears much darker than the bare metal. These BSE images allow easy quantification of oxide scale spalling (Section 4). It is seen clearly in Fig. 2 that areas of significant size are free of spalling although small spots of fresh spalls may be observed upon close examination of the large dark areas. Using SEM in the BSE mode, the evolution of spalling as a function of the number of cycles can be followed as depicted for the RT22/SCB system in Fig. 3. Comparing Figs. 2 a and b and 3c, the effect of the substrate appears clearly with much more spalling for the RT22/CMSX-4 system than for the RT22/IN792 system, RT22/SCB having an intermediate behavior.

The images in Fig. 3 show that the area of freshly spalled scale does significantly increase with the number of cycles. As for the RT22/CMSX-4 and RT22/IN792 samples (Fig. 2) it can be seen for the RT22/SCB system on Fig. 3c that areas without any extended spalling are preserved. Moreover, the images in Fig. 3 show that the size of the unspalled zones diminishes only slightly when the number of cycles is increased. However, close examination of these areas showed once again that spots of fresh spalls are often present. When looking at the whole set of micrographs, spalling may be seen as spots arranged in clusters that have a versatile shape, from elongated to blocky. The series of micrographs in Fig. 3 suggests that spalling develops both by nucleation of new clusters and by enlargement of older ones, during a single cooling event. This description is consistent with previous observations of a succession of small spalling events in a single cooling period which were measured using thermogravimetry by Evans and Lobb [22], by Bouhanek et al. [23] and recently directly observed using high speed cameras by Lours et al. [24]. This is the basis of the modelling approach described in Section 5.

4. Analysis of the experimental images

Analysis of the distribution of grey levels of the images showed a shallow minimum corresponding to the boundary between dark and white areas. This minimum was located at a grey level varying from 75 to 130 depending on the images and was used as a thresholding value. Grey tone images were thus thresholded to give binary images with spalled areas white (grey tones from the thresholding value to 255 were set to 1) and all the complementary set dark (grey tones from 0 to the thresholding value were set to 0). No attempt was made during this study to use the information contained in the grey tone distribution below the minimum, which means only the spalling related to the last cycle was considered. Fig. 4a is

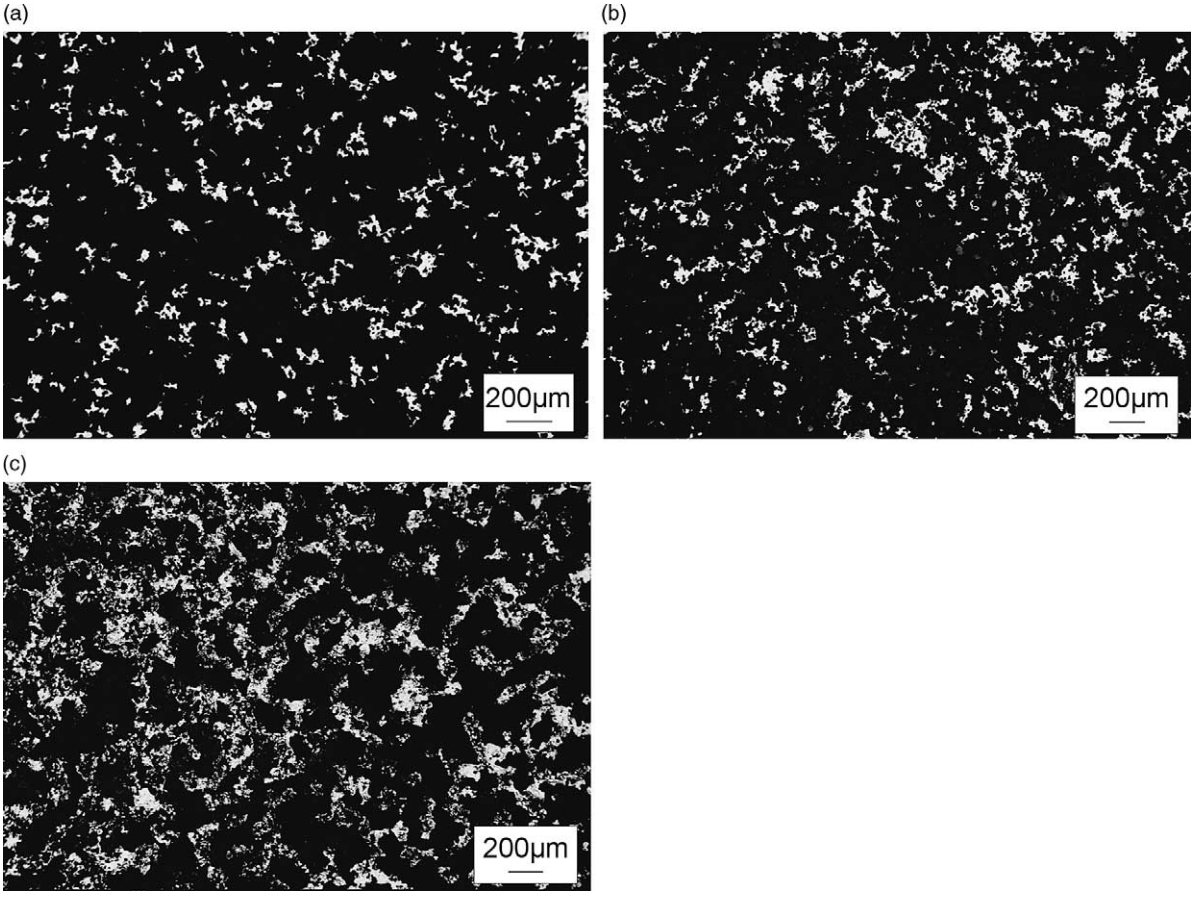

Fig. 3. SEM backscattered electron images of the surface of samples RT22/SCB after 6 (a), 17 (b) and 35 (c) cycles (note that the first image was obtained at ×40 while the two others and those in Fig. 2 were recorded at ×30).

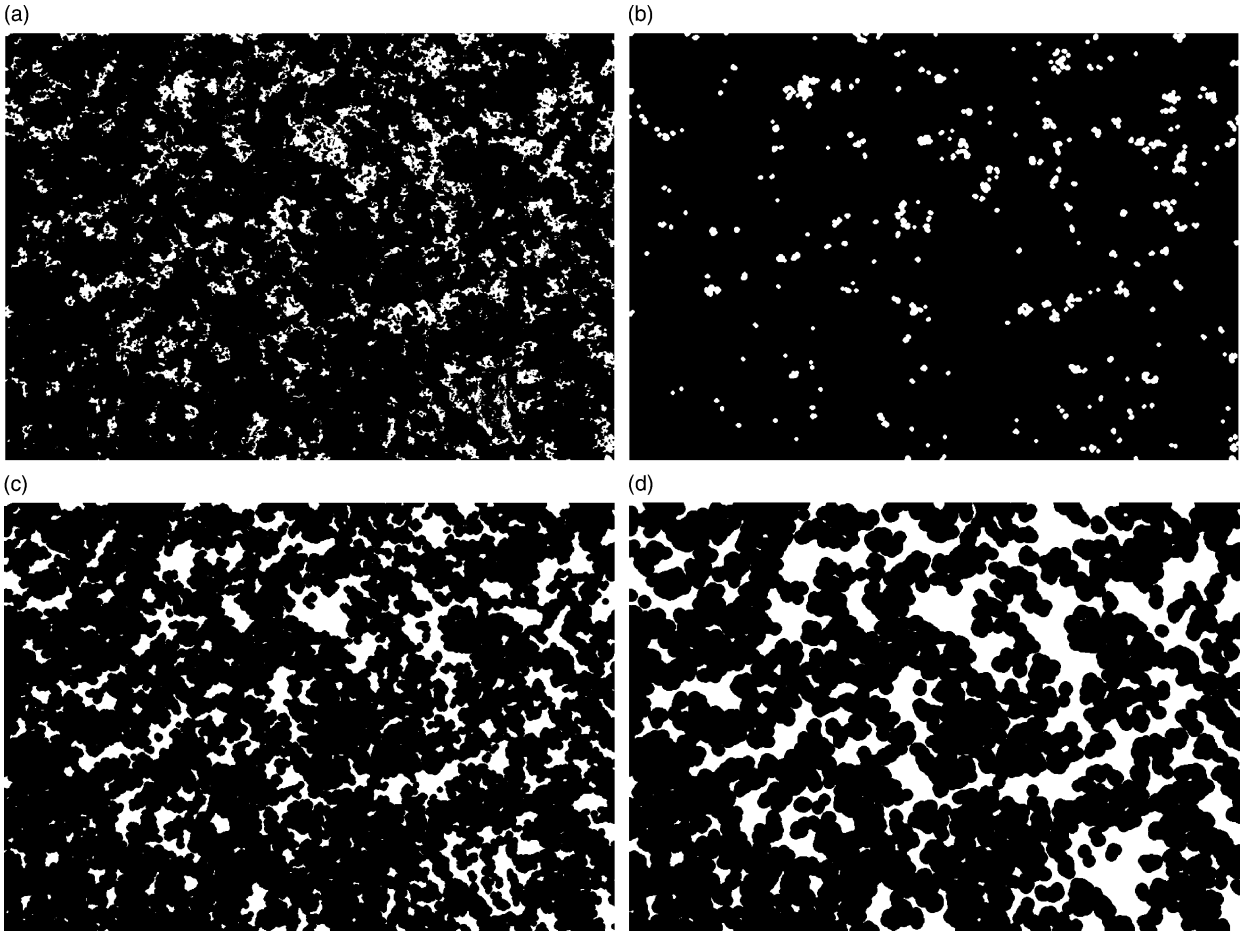

Fig. 4. (a) The image obtained by thresholding the micrograph of sample RT22/IN792 after 17 cycles of 300 h shown in Fig. 3b. (b) Shows image 4a after opening by a disc of radius 3 pixels; (c, d) Show images obtained by closing image 4a with discs of radius 5 and 10 pixels, respectively.

the image after thresholding of micrograph Fig. 3b, corresponding to the system RT22/SCB after 17 cycles.

The binary images were then transformed to characterize not only the size distribution of the spalls but also their spatial distribution. Because the connectivity of the spalled areas may change drastically from one image to another, individual analysis of the spalled areas would be meaningless. The size distribution was rather obtained by opening granulometry. Opening consists of eroding an image and then dilating the resulting image with the same structuring element as shortly described in the appendix where all the terms related to image analysis relevant to this study are defined and appropriate references indicated. Parts of the image smaller than this element disappear with erosion while those larger are reconstructed by dilation. Increasing the size of the structuring element leads to a decrease of the area left after opening until the structuring element is larger than any object present in the image. The structuring element used in the present study was a disc of varying radius. As an example, Fig. 4b shows the set resulting from opening the image in Fig. 4a with a disc 3 pixels in radius. Only blocky parts of the spalled area with minimum thickness larger than twice the disc radius (i.e. 6 pixels) remain in Fig. 4b.

Closing of an image, defined as a succession of dilations and erosions with the same structuring element, gives information on the size distribution of the elements in the complementary image. Fig. 4c and d show image 4a closed with discs of radius 5 and 10 pixels, respectively. The first closing steps link spalls within clusters. Increasing the closing size then progressively joins clusters together.

Quantitative analysis of the images thus obtained may be made with any stereological parameter. In the present case, it appeared useful to simply use the area fraction of the white zones. The data related to the three samples after 35 cycles are reported in Fig. 5, using respectively negative and positive abscissa for opening and closing. The value for a disc of zero radius is the area fraction of spalls in the experimental image. In the negative part, it is seen that the maximum radius of the spalls (i.e. the radius of the maximum inscribable disc) increases from about 20 μm for IN792 to nearly 35 μm for CMSX-4.

On the positive side, the three distributions present similar features. The area increases slowly for the first closing step, but then shows a sharp slope change, which is larger for systems RT22/CMSX-4 and RT22/SCB than for RT22/IN792. The first closing step joins spalls, which are very close to each other,

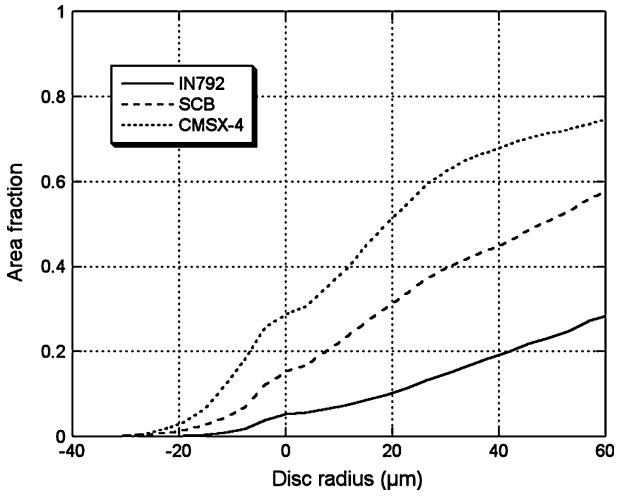

Fig. 5. Size distribution of the spalled areas (negative abscissa) and of the complementary set (positive abscissa) obtained by opening, respectively, closing, the image of samples RT22/IN792, RT22/SCB and RT22/CMSX-4 cycled 35 times.

these are mainly small spalls and the related area change is quite limited. The slope change at successive closing steps relates to the start of joining spalls in clusters and then joining clusters nearby, ending with a nearly continuous network as in Fig. 4d. The curves in Fig. 5 show finally that 70% (respectively, 40 and 25%) of the image of system RT22/IN792 (respectively, RT22/SCB and RT22/CMSX-4) is made of dark areas (i.e. without spalls) which have a minimum intercept larger than 120 μm (i.e. two times 60 μm).

Figure 6 shows the distribution curves obtained for the system RT22/SCB after 6, 17 and 35 cycles. As mentioned above, the area fraction of spalls, given by the area fraction for abscissa 0, increases with the number of cycles. The size distributions of the spalls (negative part of the curves) are all similar with a slight shift of the curves to larger sizes with increase of the cycle number. The distributions in the positive part of the curves also evolve slightly with the number of cycles with a fraction of spall-free areas of radius larger than 60 μm decreasing from 70% at 6 cycles to 40% at 35 cycles.

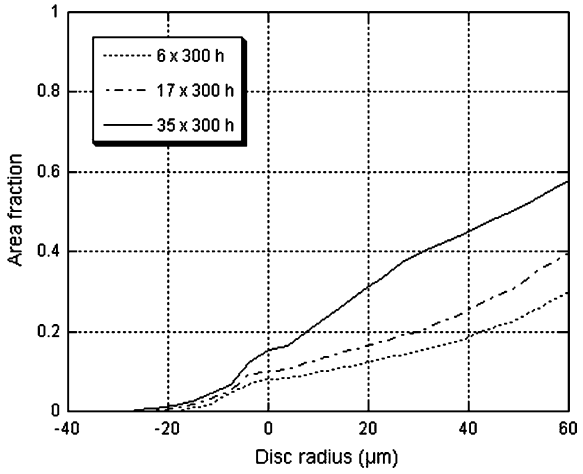

Fig. 6. Size distribution of the spalled areas (negative abscissa) and of the complementary set (positive abscissa) obtained by opening, or closing, respectively, the image of samples RT22/SCB after 6, 17 and 35 cycles.

5. Simulation

5.1. Algorithm

The observation of the micrographs in Figs. 2 and 3 together with the above description of the distribution curves shows that most of the spalls are associated in more or less elongated clusters. This suggests spalling should be simulated as a succession of two steps, nucleation and growth. Nucleation is assumed to occur at random on the surface, it is characterized by the number N_S of nucleation events. The number of pixels of the images generated for simulation was exactly the same as the size of the experimental images. Thus, the initial spalls are one pixel in diameter which is the minimum size observed experimentally as a consequence of the digitalization of the SEM images. In other words, this means that early stages of cracking of the oxide scale as determined by film mechanics are not considered since the sizes involved are much smaller than the one examined in the present work.

The first growth step consists in adding one of the 8 first neighbors on the square lattice to the seed. Each following growth step adds similarly one pixel chosen as one of the 8 first neighbors of the previously added point. The selection of the pixel to be added is made at random for each growth step. Growth is thus characterized by the number of steps N_G allowed. Fig. 7 shows examples of spalls corresponding to 250 growth steps. Because the direction of growth is chosen at random, the path followed may go back to locations previously reached. As seen in the figure, this algorithm may lead to elongated but to compact spalls as well.

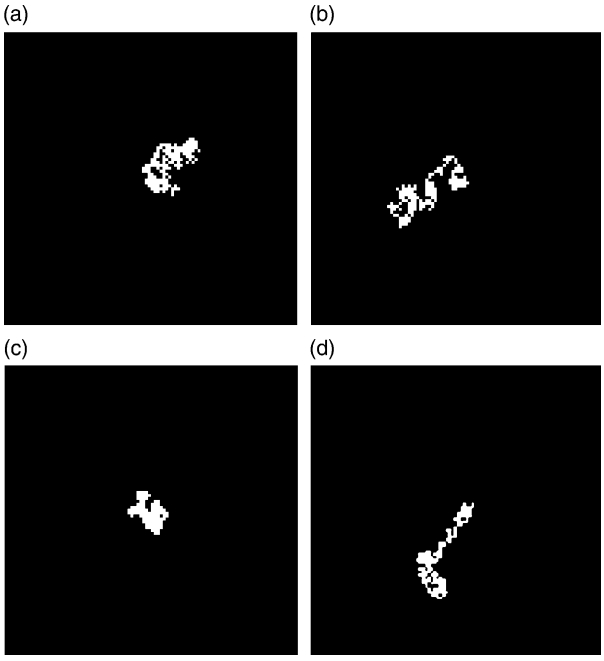

Fig. 7. Examples of spalls simulated with $N_G = 250$ growth steps shown here on a 100×100 pixel grid.

The whole algorithm consists in successively implanting N_S spalls, the number of steps of each of them being chosen at random between 0 and N_G. The size of these images in pixels was set at the same value as the experimental ones. Preliminary simulations were performed by changing the number of steps N_G at given N_S, and vice versa, such as to span the range of spall fractions measured on the experimental images. Examples of simulated images are shown in Fig. 8 where the values of N_S and N_G are indicated for each image. The series at N_S set to 500 with N_G being 250, 500 and 2500 seems to appropriately mimic the effect of cycle number in Fig. 3. Decreasing N_S to 250 while setting N_G at 500 leads to smaller clusters than those observed in Fig. 2b. Finally, increasing N_S to 2000 with the same value of N_G leads to a quite uniform coverage of the surface which cannot represent Fig. 2a.

5.2. Analysis of simulated images

These preliminary simulations thus show that the proposed algorithm with only two parameters could be

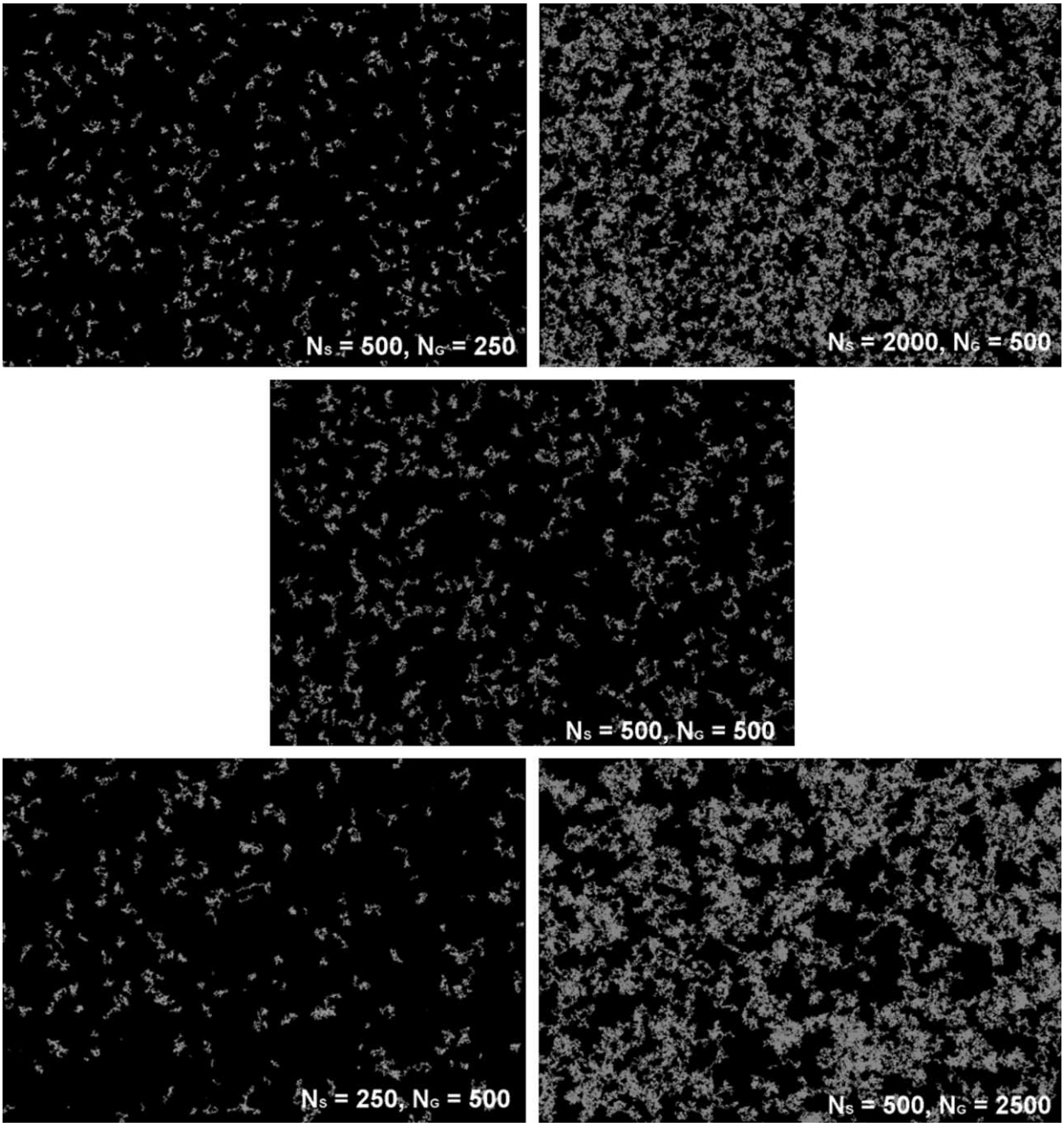

Fig. 8. Examples of simulated images for various N_S and N_G values (indicated for each image).

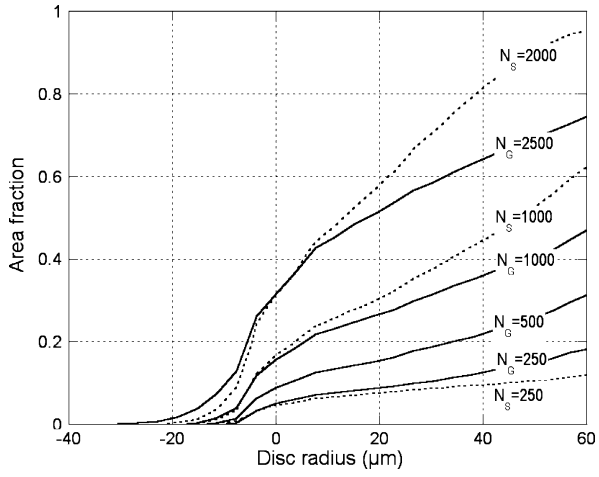

Fig. 9. Size distributions obtained by opening/closing images simulated at constant $N_S = 500$ (solid lines) and constant $N_G = 500$ (dotted lines).

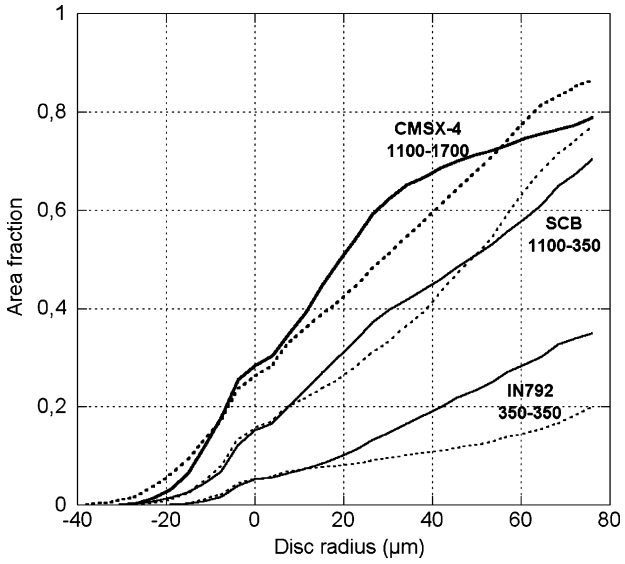

Fig. 10. Comparison of the size distribution obtained from experimental images (solid lines) for specimens cycled 35 times and on simulated images (dotted lines) for the three systems under investigation. Numbers refer to the values of N_S and N_G used for simulation.

used to simulate quite a few observations. That a given simulation does properly represent an experimental image should, however, be quantitatively checked by comparing the opening/closing distributions of experimental and simulated images. The size distributions corresponding to the images in Fig. 8 and to a few others are shown in the graph in Fig. 9. For comparison with experimental images, all pixels have been given a size of 3.8 μm. Solid lines represent curves from images with N_S set at 500, dotted curves are from images at N_G equal to 500.

Because of the high N_S and N_G values used, the curves obtained for a given set of these values are found to be highly reproducible though the corresponding images vary slightly owing to randomization. It may be noted in Fig. 9 that the curvature of the right part of the curves is negative for the highest values of N_S and N_G. This means that large areas without spalls are present and disappear only slowly as the closing size is increased. At low N_G and N_S values, the curvature is positive, but may be expected to change sign at larger abscissa. Finally, it is worth noting that the slope change at negative abscissa appears much sharper in Fig. 9 than in experimental distributions (Figs. 5 and 6). This is thought to be due to the presence of small isolated dark spots within the spalled areas of the simulated images. Such spots would not remain in place on the oxidized surface, or alternatively would not be detected as non-spalled areas on SEM images.

The next step was to look for N_G and N_S values to reproduce experimental distributions. In order to eliminate small dark spots from the spalled areas, closing with a disc of 1 pixel radius was applied to the simulated images before measurement of the size distribution. Fig. 10 compares distributions obtained from experimental and simulated images for the three samples cycled 35 times. N_S and N_G values were adjusted until the spalled fraction (abscissa 0), the maximum size of the spalls (lowest negative value) and the slope of the positive part of the distributions were all best reproduced. The discrepancies in the positive part do not have the same origin for RT22/IN792 as the two other systems. For RT22/IN792, this discrepancy is due to the fact that the predicted size of spall free areas is much larger than the actual size because of the presence of small spalls within otherwise un-spalled areas. For the other cases, the discrepancy seems to be related to the fact that spalled areas are not totally randomly distributed in the experimental images, as considered in the simulation.

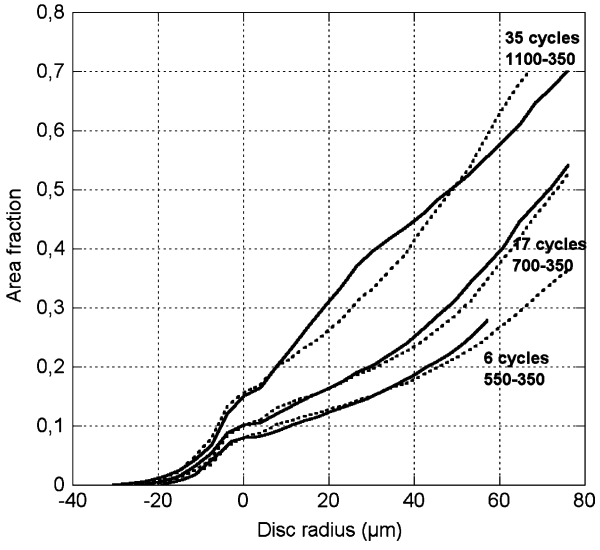

Fig. 11. Comparison of the size distribution obtained from experimental images (solid lines) for specimens of the system RT22/SCB cycled 6, 17 and 35 times and on simulated images (dotted lines). Numbers refer to the values of N_S and N_G used for simulation.

Finally, Fig. 11 compares the distributions obtained on simulated images with the experimental ones in the case of the system RT22/SCB cycled 6, 17 and 35 times. It is noted that an excellent fit is obtained for the two smaller numbers of cycles for the whole distribution, while a slight discrepancy is observed for the sample cycled 35 times as described above. Moreover, as mentioned in Fig. 11, the three simulations were performed with a value of N_G set constant at 350. An attempt was made to reproduce the distribution curves by keeping N_S at 550 and increasing the N_G values as suggested in the description relating to Fig. 8. While the distribution at negative and small positive abscissa were reproducible, the slope of the curves at the highest abscissa values was much lower than in Fig. 11, leading to a significant discrepancy with the experimental curves. Simulation thus suggests that the number of cycles leads to an increase of N_S in the present case.

6. Discussion

The first observation which can be made from the present work is the presence of areas of significant size which are free of fresh spalls. A possible explanation for such an observation would be a relation between the spalled areas and the coating microstructure. As mentioned in Section 2, the roughness of the coatings was measured for each system and it was shown that the roughness parameter R_a was similar whatever the substrate. Moreover, no connection could be made between the size of the unspalled regions and the surface profile as measured using interferometry and observed by SEM. Furthermore, from cross section observations, no link was established between spalled areas and coating grain size [1]. However, as explained in Section 2, the latter observations showed that spalling was favored by the presence of metal/oxide interfacial voids which are about 80–100 μm apart whereas unspalled zones are about 200 μm wide. Then some of the voids could be the nucleation sites for the spalling model developed in the present work. Indeed, observation of the oxidized surface after cooling suggested that spalling could occur through a nucleation and growth process of spalled areas.

The second feature of this study is that the spalling area fraction increases with the number of cycles during the first 35 cycles of 300 h at 1050 °C for the RT22/SCB system (Fig. 3). The straightforward explanation for this observation would be that the total area spalled at each cooling depends on the average oxide thickness, as suggested by many authors (e.g. [4]). Another explanation for the increase of spalling area as a function of the number of cycles is that the extent of spalling depends on the nature of the oxide formed, knowing that the scale composition varies with the number of cycles for many industrial alloys. Indeed, for the materials studied here, it was shown using XRD [1] that the relative amount of the protective alpha–alumina phase decreased with the number of cycles whereas the amounts of spinel phase and rutile phase increased, and eventually NiO appeared. It was also observed on cross sections that the oxide scale thickness increased between 6 and 17 cycles (from 3.4 μm to 10 μm) but no longer between 17 and 35 cycles when the first stationary regime kinetics is reached, during which alumina is the growth rate controlling oxide. The explanation of an increase of spalling area with the average oxide thickness is consistent with the higher spalling area for the 17th cycle in comparison with the 6th, but it does not explain the increase in spalling between the 17th and the 35th cycles. The increase of spalling at 35 cycles is more likely due to the change in the composition of the oxide scale which contains much more spinel phase.

A complementary or alternative explanation for the increase of spalling as a function of the number of cycles is the increase in the number of interfacial voids at the metal/oxide interface which was evidenced in the experimental study [1]. This last explanation is consistent with the present simulation which shows that the effect of the number of cycles may be described by an increase of the number of nucleation sites N_S (Fig. 11). This is also consistent with the observation that N_S is lower for the system RT22/IN792 (Fig. 10) for which the number of interfacial cavities was found to be lower than for RT22/CMSX-4 and RT22/SCB [1].

The third point of the discussion concerns the succession of spalling in a single cooling event which was not taken into account in previous kinetic models which assume a uniform (random) distribution of spalls over the oxidized surface, whether the extent of spalling remains unchanged with time [8,11] or depends on oxide scale thickness [9,13]. The succession of spalling events during a single cooling is not yet described in the more recent 2D Monte Carlo simulations initiated by Strehl [12] and currently developed by Sureau et al. [25] although this could be easily considered. On the contrary, such a time-dependent phenomenon is implicitly accounted for in the present approach through the nucleation and growth stages, though only the resulting geometrical features have been described. In that respect, the fact that the path followed by a spall goes back to positions previously encountered does not appear to be of any importance. This means that not all the virtual growth steps do effectively lead to an increase of the size of the spall. Further, the agreement obtained between simulated and experimental images strongly suggests that spalling results from multi-cracking of the oxide scale. Relaxation by spalling during the growth stage may thus be seen as in a crack propagation process. Ahead of the crack, stresses build up until a certain level is reached which leads to a propagation over some distance which is of constant size (pixel size) in the present algorithm.

7. Conclusion

During the long term (10,500 h) cyclic oxidation at 1050 °C, NiPtAl-RT22 coatings experience partial spalling of the grown oxide scale. The extent and morphology of the spalled areas were analyzed with backscattered electron imaging of samples cooled after 6, 17 and 35 cycles of 300 h each at 1050 °C in still laboratory air. The extent of spalling was found to increase with the number of cycles and also to depend on the nature of the substrate. The increase of the spalled area, after cooling,

with the number of cycles cannot be explained only by an increase of the average oxide scale thickness and may also depend on the oxide scale composition and/or on the number of interfacial voids [1].

Analysis of the images of the spalled samples suggested a simulation of spalling should be developed that accounts for nucleation and growth of spalls during each single cooling. A model was developed using two parameters N_S and N_G which quantify the number of nucleation sites on the surface and the maximum number of growth steps for each spall respectively. Values of N_S and N_G were found which satisfactorily reproduce the size distributions of the spalled and unspalled surface areas for each of the samples analysed. The simulation of the spalling of system RT22/SCB showed that the number of growth steps did not change while the number of nucleation sites increased with the number of cycles. This can be related with the experimental observation of voids appearing at the metal/oxide interface. Some of these voids could act as nucleation sites for spalling. This description is also consistent with the fact that the nucleation parameter N_S is found to be lowest for the RT22/IN792 system for which fewer interfacial voids were observed.

This nucleation and growth simulation of spalling could be applied to the direct in situ observations of spalling (high speed cameras, themogravimetry during cooling) with varying cooling conditions. It could also to be combined with an oxide growth model to reproduce the overall kinetics of cyclic oxidation.

Acknowledgements

The authors thank the EEC through the European project Allbatros (N°ENK5-CT2000-00081). They also appreciated discussions with Alain Hazotte (LETAM, Metz) on image analysis and simulation. The authors are pleased to acknowledge Mireille Lacaze for the authorization to reproduce and distort her painting (Fig. A1a).

Appendix A. Basic notions on image transformations based on mathematical morphology

Numerical images are made of 'pixels' (for picture element) most often arranged on a square lattice, each pixel having its own colour or grey level. Such images may conveniently represent an observed set of objects (hereafter, denoted 'phase') provided the distance between pixels (numerical resolution) is small enough. As a matter of fact, desktop computers are nowadays able to handle images large enough so that the contours of the objects appear smooth. In the following illustrations, these contours will therefore be represented as continuous.

As is the case in the present study, phase quantification is often performed on binary images obtained from grey-tone ones by thresholding. This transformation separates the image into two parts, a set of pixels representing the phase of interest and which are given a value of 1 and the complementary set with pixels set at 0. Fig. A1a and b show, respectively, a grey tone image with interconnected objects in dark contrast and the resulting threshold image where the selected phase appears white. When the phase is composed of isolated objects, their size distribution, or 'granulometry', is easily obtained by measuring a size parameter (area, mean or equivalent diameter, etc.) on each of them [26]. However, this is no longer possible when the phase is composed of erratic interconnected objects. In such cases, Matheron [27] and Serra [28] proposed to use a filtering procedure called 'opening granulometry'. Its presentation requires the terms 'structuring element', 'erosion' and 'dilation' to be defined. They are basic concepts of the field of mathematical morphology initiated by these authors.

A structuring element (SE) is an object characterised by its shape and by a specified point (e.g. the centre of gravity) called 'application point'. Although the SE can have any shape, it is usual to use simple ones (e.g. the white circle B in Fig. A1b). In the case of numerical images, structuring elements are built from appropriate sets of pixels and can be doublets of points, linear segments, discs, etc. Erosion of a phase (an image) by a given structuring element, consists in positioning the selected structuring element on all the points (pixels) associated with the set of objects and keeping only the points (pixels) for which the structuring element is wholly included in the phase. The image resulting from the erosion of the set in Fig. A1b by the structuring element B is shown in Fig. A1c. Dilation of the image consists in positioning the structuring elements on all the pixels of the complementary image and keeping only the points (pixels) for which the structuring element hits the phase. The image resulting from the dilation of the initial image A1b is shown in Fig. A1d. The transformation called *opening* is the combination of an erosion then a dilation with the same structuring element. The result is shown in Fig. A1e. The difference between this latter image and the initial one relates to the part of the initial image with a size smaller than the disc diameter. Similarly, dilation then erosion define the transformation called 'closing', which is illustrated in Fig. A1f. Closing is the dual transformation of opening, i.e. closing an image is just opening the complementary set. The difference with the initial image shows part of the complementary set with a size lower than the disc diameter.

When increasing the size of the structuring element, less and less area of the initial set of objects remains after opening, while less and less of the complementary image remains after closing. Consequently, opening or closing, increasing the size of the structural element acts much like successive sieves used to separate particles of various dimensions. The main advantage of the method is that it applies to continuous medium as well as to separate particles. Matheron [27,29] showed that a granulometry may be defined on the basis of opening, i.e. that the properties of this set transformation are strong enough to unequivocally define size distributions. More details on opening granulometry and other aspects of applied mathematical morphology can be found in various text books [30–32].

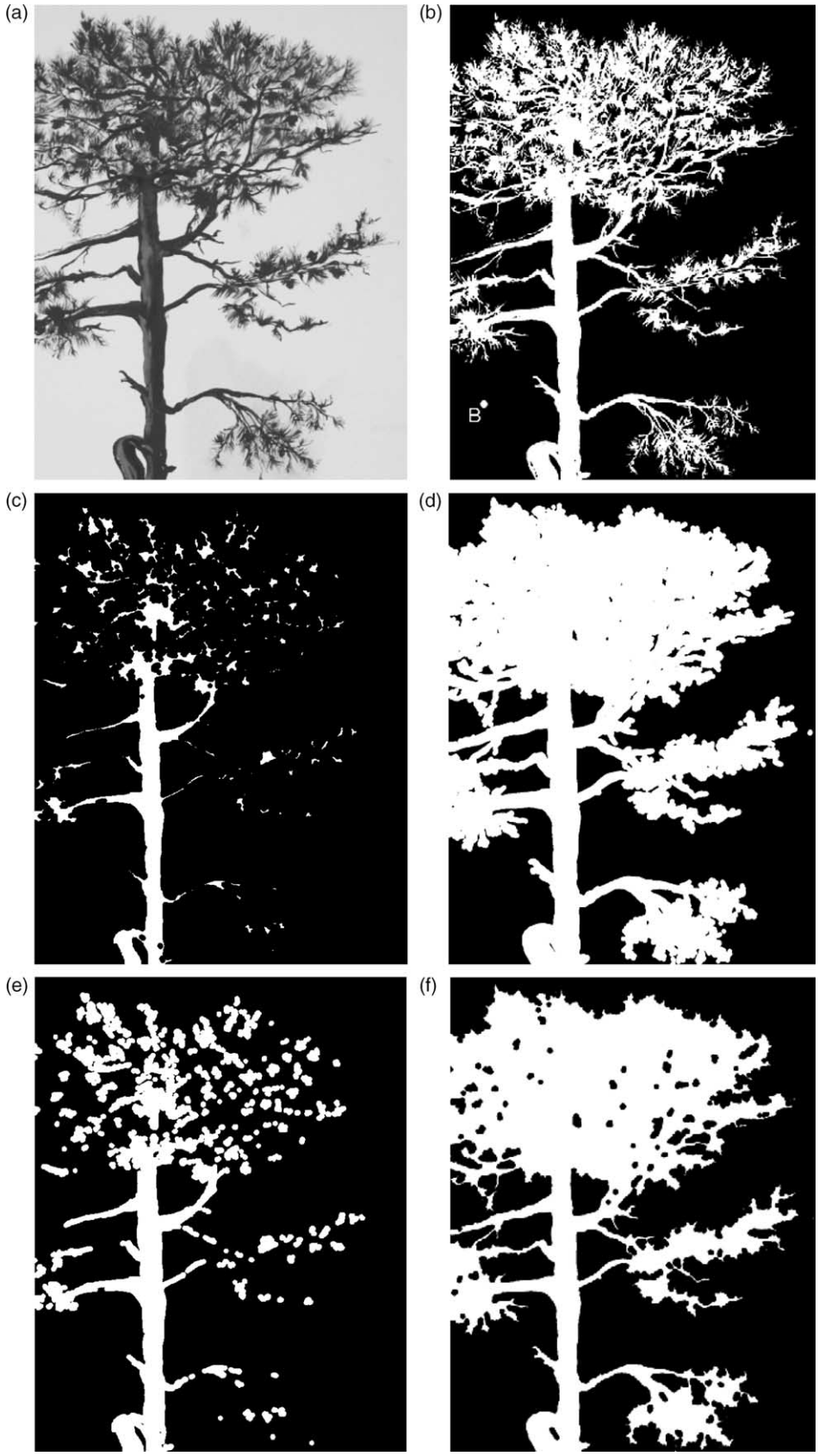

Fig. A1. (a) Example of a grey-tone image with interconnected objects in dark contrast; (b) Binary image obtained by thresholding image a, showing also a disc B of 7 pixels in radius to be used as structuring element; (c, d) images obtained by eroding, respectively, dilating, image b with B; (e, f) images obtained by opening, respectively closing, image b with B.

References

[1] Vialas N, Monceau D, Oxid Metals, Submitted for publication.
[2] Kofstad P. High temperature corrosion. London: Elsevier; 1988.
[3] Dryepondt S, Andrieu E, Monceau D, Crabos F, Vernault C. Mater Sci Forum 2004;461–464:647–54.
[4] Evans HE. Int Mater Rev 1995;40:1–40.
[5] Jedlinski J, Bennet MJ, Evans HE. Mater High Temp 1994;21:169–75.
[6] Pint BA, Tortorelli PF, Wright IG. Oxid Metals 2002;58:73–101.
[7] Barrett CA, 'COREST,' Report No. NASA-TN-D-8132 E-8432 1976.
[8] Smialek JL. Metall Mater Trans A 1978;9:309–19.
[9] Lowell CE, Barrett CA, Palmer RW, Auping JV, Probst HB. Oxid Metals 1991;36:81–112.
[10] Moon CO, Lee SB. Oxid Metals 1993;39:1–10.
[11] Poquillon D, Monceau D. Oxid Metals 2003;59:409–31.
[12] Strehl G. Über Verarmungsprobleme bei der Oxidation von Hochtemperaturlegierungen am Beispiel des Systems Fe-20Cr–5Al, PhD thesis, Universität Clausthal 2002.
[13] Smialek J. Acta Mater 2004;52:2111–21.
[14] Evans AG, Hutchinson JW. Int J Solids Struct 1984;20:455–66.
[15] Evans HE. Mater High Temp 1994;12:219–27.
[16] Chan KS. Metall Mater Trans A 1997;28:411–22.
[17] Evans AG, Hutchinson JW, He MY. Acta Mater 1999;47:1513–22.
[18] Vialas N, Monceau D, Pieraggi B. Mater Sci Forum 2004;461–464: 747–54.
[19] Poquillon D, Oquab D, Viguier B, Senocq F, Monceau D. Mater Sci Eng A 2004;381:237–48.
[20] Caron P, Escalé A, McColvin G, Blacker M, Wahi R, Lelait L. Proceedings of the fifth international charles parsons turbine conference: Parsons 2000—advanced materials for 21st century turbines and power plants, Cambridge; UK; 2000.
[21] Angenete J, Stiller K, Langer V. Oxid Metals 2003;60:83–101.
[22] Evans HE, Lobb RC. In Proceedings of EUROCORR87: 1987.p. 135–40.
[23] Bouhanek K, Oquab D, Pieraggi B. Mater Sci Forum 1997;251–254: 33–40.
[24] Lours P, Maoult YL, Adé D, Pieraggi B. Mater Sci Forum 2004;461–464: 639–46.
[25] Sureau S, Oquab D, Poquillon D, Salabura JC, Monceau D. unpublished results.
[26] DeHoff RT, Rhines FN. Quantitative microscopy. New-York: McGraw Hill; 1968.
[27] Matheron G. In Eléments pour une théorie des milieux poreux. Paris: Masson et Cie.; 1967.
[28] Serra J. Image analysis and mathematical morphology. London: Academic Press; 1982.
[29] Matheron G. J Microscopy 1972;93:15.
[30] Coster M, Chermant J-L. Précis d'analyse d'images. Presses du CNRS; 1989.
[31] Soille P. Morphological image analysis. Berlin: Springer; 1999.
[32] Ohser J, Mücklich F. Statistical analysis of microstructure in materials science. In: Barnett V, editor. Chichester: Wiley.